Applied Energy 361 (2024) 122958

Contents lists available at ScienceDirect

Applied Energy

journal homepage: www.elsevier.com/locate/apenergy

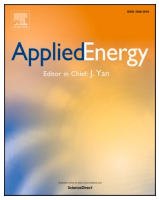

Analysis on a single-stage direct-coupled thermoacoustic refrigerator driven by low/medium-grade heat

Yiwei Hu [a,b], Jingyuan Xu [c,*], Dan Zhao [d], Rui Yang [a], Jianying Hu [a,b], Ercang Luo [a,b,**]

[a] Key Laboratory of Cryogenic Science and Technology, Technical Institute of Physics and Chemistry, Chinese Academy of Sciences, Beijing 100190, China
[b] University of Chinese Academy of Sciences, Beijing 100049, China
[c] Institute of Microstructure Technology, Karlsruhe Institute of Technology, Karlsruhe 76344, Germany
[d] Department of Mechanical Engineering, Faculty of Engineering, University of Canterbury, Private Bag 4800, Christchurch 8041, New Zealand

HIGHLIGHTS

- A thermoacoustic refrigerator using low/medium-grade heat is proposed for domestic cooling.
- The increased mean pressure plays a favorable role in reducing the onset temperature difference.
- The refrigerator achieves a cooling efficiency 0.24 to 0.61 at cooling temperatures of −23 °C to 7 °C.
- Single-cavity structure outperforms multi-cavity structures in terms of cooling performance.
- The refrigerator compensates deficiencies of current heat-driven cooling at low temperatures.

ARTICLE INFO

Keywords:
Thermoacoustic refrigerator
Thermoacoustic
Heat-driven cooling
Low grade heat
Domestic cooling

ABSTRACT

Cooling for domestic applications using low/medium-grade heat sources is essential to reduce CO_2 emissions and promote environmental friendliness. Thermoacoustic technology is quite promising to meet such demand. This paper proposes a compact and highly efficient single-stage thermoacoustic refrigerator for utilizing low/medium-grade heat source. It is different from conventional design by containing only one thermoacoustic core unit and enhancing cooling efficiency by improved acoustic matching incorporating a cavity structure with no less cooling performance than a multi-unit thermoacoustic refrigerators. For this, a matrix transfer method based on thermoacoustic theory is applied to investigate the onset characterizes of the thermoacoustic cooling system. The present results reveal that the lowest onset temperature difference of 62 K can be achieved when using nitrogen as the working gases. Steady-state characteristics of the system are then investigated, including the exergy loss analysis, the axial distributions of key parameters, cooling performance under different working conditions and mixed working gases. The analysis based on the introduced cavity is subsequently done in terms of the position, volume, and quantity of cavity. Further comparisons are made between the single-cavity and multi-cavity structures, demonstrating a superior performance of the single-cavity structure. Finally, the proposed thermoacoustic refrigerator is compared with existing heat-driven cooling technologies. The results demonstrate that the thermoacoustic refrigerator can compensate the deficiencies of the existing heat-driven cooling technologies at low cooling temperatures.

1. Introduction

The worldwide desire for energy conservation and emission reduction has drawn attention to the utilization of low/medium-grade thermal energy such as renewable thermal energy (solar and geothermal) [1,2] and waste heat from industrial processes [3]. A reasonable recovery of waste heat has the potential to improve energy efficiency of energy systems by 10–50% [4]. Meanwhile, heating and cooling systems in buildings account for 30–50% of global energy

* Corresponding author at: Institute of Microstructure Technology, Karlsruhe Institute of Technology, Karlsruhe 76344, Germany.
** Corresponding author at: Key Laboratory of Cryogenic Science and Technology, Technical Institute of Physics and Chemistry, Chinese Academy of Sciences, Beijing 100190, China.
E-mail addresses: jingyuan.xu@kit.edu (J. Xu), ecluo@mail.ipc.ac.cn (E. Luo).

https://doi.org/10.1016/j.apenergy.2024.122958
Received 10 November 2022; Received in revised form 27 October 2023; Accepted 1 March 2024
Available online 6 March 2024

Nomenclatures[11]

Symbols

a	acoustic speed, m s^{-1}
A	working gas area, m^2
c_p	specific heat capacity, J kg^{-1} K^{-1}
C	acoustic compliance, m^3 Pa^{-1}
d_h	hydraulic diameter, m
D	diameter, m
e	mass-specific total gas energy, J kg^{-1}
E	minor losses in the U-shaped tube
f	frequency, Hz
f_D	Darcy friction factor
f_υ	spatial averaged viscous function
f_κ	spatial averaged thermal function
F	viscous pressure gradient
g	acceleration of gravity, m s^{-2}
i	imaginary symbol
k	thermal conductivity, W m^{-1} K^{-1}
k_g	gas conductivity, W m^{-1} K^{-1}
K	spring constant, N m^{-1}
K_{los}	total local loss coefficient
l	length, m
N_k	axial conductivity enhancement ratio
Nu	Nusselt number
y_0	half of the plate spacing, m
n	stage number
P	pressure, Pa
P_1	the amplitude of the first-order pressure wave, Pa
Pr	Prandtl number
q	instantaneous axial heat flux, W m^{-2}
q_w	heat fluxes between gas and solid
q_x	heat fluxes inside the gas or solid
Q_w	heat flow per unit length, W m^{-1}
Q	rate at which heat is transferred, W
r	acoustic power loss ratio
r_h	hydraulic radius, m
r_t	tube radius, m
R_m	mechanical damping coefficient, N m s^{-1}
S_x	wetted perimeter
T	temperature, K
T_0	normalization temperature, K
T_m	mean temperature, K
T_w	temperature between gas and solid, K
T_x	temperature inside the gas or solid, K
u	mean-flow velocity, m s^{-1}
U_1	the first-order volume flow rate, m^3 s^{-1}
V	volume, m^3
W	acoustic power, W
y_0	half of the channel width of the heat exchanger, m
η	thermoacoustic efficiency
γ	specific heat ratio
ω	angular frequency, s^{-1}
ρ_m	mean density, kg m^3
κ	thermal diffusivity, m^2 s^{-1}
υ	kinematic diffusivity, m^2 s^{-1}
δ	penetration depth, m
μ	dynamic viscosity, kg m^{-1} s^{-1}
$\mu_{g,0}$	gas dynamic viscosity at ambient temperature, kg m^{-1} s^{-1}
Φ	porosity of the regenerator
τ	absolute temperature ratio at two extremes of the regenerator
θ	phase angle, °
δ_κ	thermal diffusion depth, m
δ_v	viscous diffusion depth, m
$\|\ \|$	determinant of the matrix

Abbreviations

AE_{fric}	flow friction losses, W
AE_{Qw}	non-ideal heat transfer losses, W
AE_{Qx}	axial heat flow losses, W
AHX	ambient-temperature heat exchanger
CHX	cooling heat exchanger
COP	Coefficient Of Performance
HX	heat exchanger
HHX	high-temperature heat exchanger
PT	pulse tube
REG	regenerator
TBT	thermal buffer tube

Subscripts

a	ambient
c	cooler/cooling
e	engine
g	gas
h	heating
in	inlet/import
m	mean
sub	subunit
κ	thermal
υ	viscous
Δ	difference
∇	gradient

consumption, thus an increase in the efficiency of energy systems would mean a significant reduction in global energy consumption [5,6]. VCR (vapor compression refrigeration) is still one of the most widely used refrigeration technologies in the domestic cooling [7], whose extensive use of fluorinated refrigerants has caused problems of carbon emissions. It is therefore crucial to require a carbon-neutral and sustainable alternative cooling system that can recover waste heat, especially low/medium grade heat energy.

As an emerging energy conversion technology, thermoacoustic technology is a major area of interest within the field of heat-driven applications that can be used for heating [8,9], cooling [10,11], and power generation [12]. Thermoacoustic cooling owns remarkable advantages of low vibration and high reliability due to no mechanical moving parts, and environmental-friendly features because of using pollution-free working gas. In addition, thermoacoustic refrigerators can utilize heat sources, especially low/medium-grade waste heat sources [13], and feasible ways of utilizing such heat sources include electric heating [14], heat transfer from thermal oil [15], and solar collector panels for heat supply [16]. Up to now, thermoacoustic technology has been able to obtain kilowatt-scale cooling capacity in the room-temperature cooling temperature zone [14,15], which shows promising perspectives in the domestic cooling fields.

Numerous research has been conducted to improve the cooling performance of the thermoacoustic refrigerator in the past decades. In 1991, Radebaugh et al. [17] first developed a thermoacoustic refrigerator driven by a thermoacoustic engine, with no mechanical moving parts. In 1999, Backhaus et al. [18] presented a thermoacoustic engine that attained an acoustic power of up to 710 W with a thermal power conversion efficiency of 30%, which promoted the development of thermoacoustic refrigerators driven by thermoacoustic engines. In 2006,

Luo et al. [19,20] introduced a heat-driven thermoacoustic refrigerator, which obtained a cooling power of 250 W. In 2009, Li et al. [21] tested a heat-driven thermoacoustic refrigerator, which achieved a cooling power and cooling efficiency of 469 W and 0.216, respectively. In 2017, Hasegawa et al. [22] proposed a multistage-engine-driven thermoacoustic refrigerator, which obtained a cooling efficiency of 0.029 at a cooling temperature of −50 °C.

A commonality lies in the thermoacoustic systems mentioned above, which is that their regenerators are dominated by the traveling-wave acoustic fields while the resonant-tubes are still dominated by standing-wave acoustic fields. The loop-type structure is a development direction to improve the performance of the traveling-wave thermoacoustic systems, which means both the regenerators and resonant-tubes are dominated by the traveling-wave acoustic fields. The original report on looped structure was an acoustic cooler proposed by Yazaki et al. in 2002 [23]. In 2008, De Blok et al. [24] arranged multiple thermoacoustic conversion units in a single looped tube to efficiently increase the power density. The subsequent proposal for a four-stage looped thermoacoustic cooler achieved a relative Carnot efficiency of 13% [25]. In addition to improving cooling efficiency, reducing the number of energy-conversion units while studying proper acoustic field matching is a key development direction. In 2019, Wang et al. [15] presented a three-stage looped heat-driven thermoacoustic refrigerator with direct-coupled configuration, which achieved a cooling power of 3.3 kW with a cooling efficiency of 0.22 using low/medium-grade waste heat. In 2022, Yang and Chi et al. [9,14] further reduced the number of thermoacoustic core units to 2 based on the three-stage system, which obtained a cooling power of 3.9 kW with a cooling efficiency of 0.3. In 2021, Ding et al. [26] proposed a two-stage interval-type thermoacoustic refrigeration system for waste heat utilization, obtaining a maximum cooling power of 0.95 kW. As for the single-unit based thermoacoustic systems, Jin et al. [27] analyzed the effect of the cavity structures on the acoustic fields in the context of a single-unit thermoacoustic prime mover in 2016, which provided ideas for later research on the single-unit looped thermoacoustic system. In 2018, Saechan et al. [28] developed a heat-driven thermoacoustic cooler, featuring interval-type arrangement of engine and cooler units in a loop, along with assisted modulation of the system acoustic field by stub and piston devices, ultimately yielding 7 W of cooling at 8 °C. In 2020, Farikhah [29] performed theoretical calculations for a heat-driven single-stage interval-type thermoacoustic cooler and derived an onset temperature of 580 K at 3 MPa. Additionally, the novel heat-driven thermoacoustic cooler with gas-liquid resonators proposed by Xu et al. [30] in 2020 provides another development direction to improve the acoustic filed matching. Calculation results show a significant improvement in cooling power and efficiency of 5.6 and 1.5 times, respectively, compared to conventional gas resonant-tube systems.

The existing heat-driven thermoacoustic refrigerators currently face problems including: 1) They typically consist of multiple thermoacoustic core units in a loop, resulting in complex systems, as well as the complexity of integrating the thermoacoustic systems with subsystems (e.g., cooling water system) thus preventing their practical applications; 2) Multi-unit systems reportedly suffer from inconsistent working conditions across individual unit and the easy rupture of the elastic membrane in the loop that suppresses direct current, which further impede long-term and stable operation; 3) Some heat-driven single-unit thermoacoustic refrigerators have been established [28,31], but their interval-type arrangement and inappropriate acoustic fields matching leads to relatively low system performance, not showing promising application prospects. It has been shown that direct-coupled-type structures are superior in terms of cooling efficiency and power density [32]; 4) The introduction of the mechanical moving parts in some previously proposed systems would somewhat compromise the advantages of high reliability and long lifespan of thermoacoustic systems. To address these problems, the present work supplements heat-driven looped traveling-wave thermoacoustic system related literature with several novel insights.

- The first contribution of this study is the introduction of a single-stage direct-coupled thermoacoustic refrigerator, characterized by its unique combination of a single unit and a direct-coupled design, which reduces the thermoacoustic core unit to one and performs no less well than the multi-unit systems.
- A cavity structure is innovatively incorporated to this system at appropriate location to enhance the acoustic matching, as a complement to the phase-modulating configuration. Furthermore, without introducing any mechanical moving parts, the system presented in this paper retains the advantages of high reliability and long lifespan while realizing the optimal system performance among the reported single-unit looped thermoacoustic refrigeration systems.
- A comprehensive analysis is investigated, including the onset characteristics, cooling performance, acoustic field characteristics, and the analysis based on the introduced cavity structure including the influence of the position, volume, and quantity of cavity.
- This is the first study that examines the comparative analysis with existing heat-driven cooling technologies from a standpoint to the cooling power and efficiency, showing promising prospects for the thermoacoustic cooling technologies on room-temperature cooling applications.

2. Configuration description and working principle

Fig. 1 presents the schematic of a looped single-stage heat-driven thermoacoustic refrigerator. The refrigerator consists of a simple direct-coupled energy-conversion core unit and a gas resonator unit connected and forming a loop. The core unit includes an engine stage and a cooler stage. The engine stage consists of an ambient-temperature heat exchanger (AHXe), a regenerator (REGe), a high-temperature heat exchanger (HHXe), and a thermal buffer tube (TBTe). The cooler stage consists of an ambient-temperature heat exchanger (AHXc), a regenerator (REGc), a cooling-temperature heat exchanger (CHXc), and a pulse tube (PTc).

The thermoacoustic refrigerator works as follows: the HHXe is heated by a medium/low-grade heat, while the AHXe is maintained at room temperature by the cooling water, thus generating a temperature gradient the REGe. As the axial temperature gradient exceeds a threshold value, self-excited thermoacoustic oscillation begins and the conversion from thermal energy to acoustic power occurs in the engine stage. The amplified acoustic power is then consumed in the cooler stage to produce cooling power, and the remaining acoustic power is recycled down the loop back to the engine stage, and the cycle is repeated. Table 1 shows the optimized geometric dimensions of the main components of the system, which is determined based on the experience of our previous studies and the combined optimization of cooling capacity and efficiency.

The first novelty of this system setup is the reduction of the number of core units to one compared to the conventional heat-driven thermoacoustic refrigerators, which largely reduces the complexity and improves the compactness and stability of the system. The second innovation is the introduction of a cavity structure at the appropriate location of the gas resonator unit, which enhances the acoustic matching and provides suitable acoustic fields for the thermoacoustic refrigerator.

[1] The description of quantities under the equations are shown only in the nomenclature.

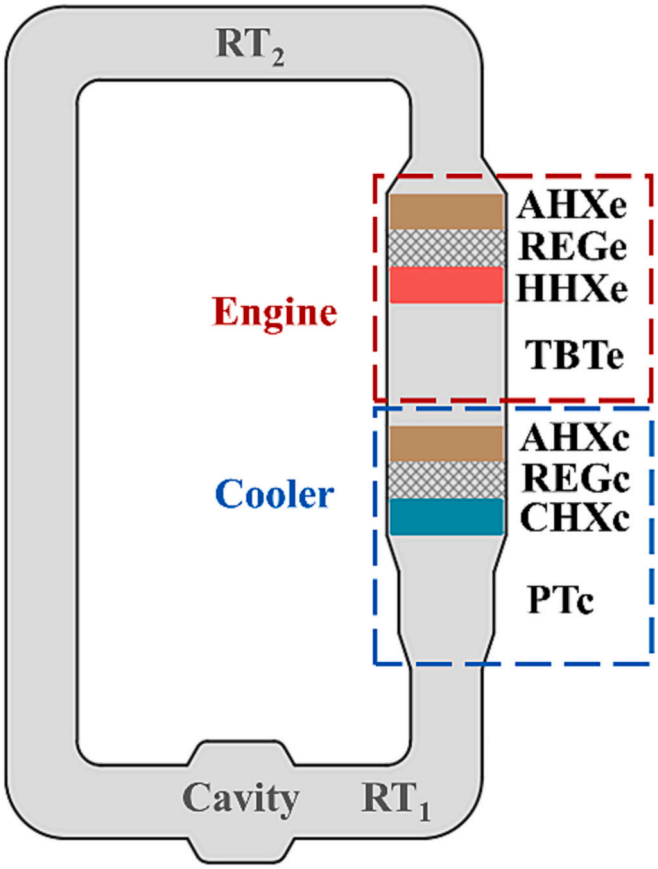

Fig. 1. Schematic of a looped single-stage heat-driven thermoacoustic refrigerator with one cavity. AHX is the ambient-temperature heat exchanger, REG is the regenerator, HHX is the high-temperature heat exchangers, TBT is the thermal buffer tube, CHX is the low-temperature heat exchanger, PT is the pulse tube, and RT is the resonant-tube. e is for the engine, and c is for the cooler.

Table 1
Dimensions of the components in each subunit.

Subunit	Parts	Diameter (mm)	Length (mm)	Other dimensions
Engine	AHXe	180	35	Shell-tube type, 12% in porosity, 1 mm in internal diameter
	REGe	180	35	77% in porosity, 50 μm in wire diameter
	HHXe	180	35	Shell-tube type, 12% in porosity, 1 mm in internal diameter
	TBTe	180	100	7 mm in wall thickness
Cooler	AHXc	180	35	Shell-tube type, 12% in porosity, 1 mm in internal diameter
	REGc	180	35	79% in porosity, 50 μm in wire diameter
	CHXc	180	35	Shell-tube type, 12% in porosity, 1 mm in internal diameter
	PTc	90	50	7 mm in wall thickness
Resonator	RT_1	55	1800	
	Cavity	126	500	1.5 mm in wall thickness
	RT_2	55	9100	

3. Methods and validations

3.1. Frequency-domain model description

This section focuses on the method of the onset characteristics analysis of the looped single-stage heat-driven thermoacoustic refrigerator by using the transfer matrix method based on linear thermoacoustic theory [33]. For the working gas regions, the matrix type of the linearized conservation equations of momentum and mass can be formulated as

$$\frac{d}{dx}\begin{pmatrix} P_1(x) \\ U_1(x) \end{pmatrix} = Z\begin{pmatrix} P_1(x) \\ U_1(x) \end{pmatrix} \tag{1}$$

$$Z = \begin{pmatrix} 0 & -\frac{1}{A}\frac{i\omega\rho_m}{1-f_v} \\ -\frac{i\omega A[1+(\gamma-1)f_\kappa]}{\gamma P_m} & \frac{f_\kappa - f_v}{(1-f_v)(1-Pr)}\frac{1}{T_m}\frac{dT_m}{dx} \end{pmatrix} \tag{2}$$

The transmitted matrix **M** with the length component l can be acquired as:

$$\begin{pmatrix} P_1(x+l) \\ U_1(x+l) \end{pmatrix} = M\begin{pmatrix} P_1(x) \\ U_1(x) \end{pmatrix} \tag{3}$$

In the heat exchanger, Eqs. (1) and (2) can be solved due to $\frac{dT_m}{dx} = 0$. The transmitted matrix of the heat exchanger $\mathbf{M_{HX}}$ can be written as

$$\mathbf{M_{HX}} = \begin{pmatrix} cos(kl) & -\frac{i\omega\rho_m sin(kl)}{A_{gas}k(1-f_v)} \\ \frac{A_{gas}k(1-f_v)sin(kl)}{i\omega\rho_m} & cos(kl) \end{pmatrix} \tag{4}$$

where k is the complex wavenumber and can be expressed as

$$k = \frac{\omega}{a}\sqrt{\frac{1+(\gamma-1)f_\kappa}{1-f_v}} \tag{5}$$

For a plate-fin type heat exchanger in the system,

$$f_\kappa = \frac{tanh[(1+i)y_0/\delta_\kappa]}{(1+i)y_0/\delta_\kappa} \tag{6}$$

$$f_\nu = \frac{tanh[(1+i)y_0/\delta_\nu]}{(1+i)y_0/\delta_\nu} \tag{7}$$

where δ_κ and δ_ν can be written as

$$\delta_\kappa = \sqrt{\frac{2\kappa}{\omega}}, \delta_\nu = \sqrt{\frac{2\nu}{\omega}} \tag{8}$$

In the thermal buffer tube, pulse tube, and cavity structure, the (2,2) element of **Z** ($\mathbf{Z}_{22}$) in Eq. (2) is approximately zero since the f_k and f_v are very small in value because of the large diameter [34]. The transmission matrix of the thermal buffer tube or pulse tube $\mathbf{M_{TBT/PT/CVT}}$ can be written as

$$\mathbf{M_{TBT/PT/CVT}} = \begin{pmatrix} 1 & 0 \\ -\frac{i\omega V}{\gamma P_m} & 1 \end{pmatrix} \tag{9}$$

In the regenerator, $\frac{dT_m}{dx} \neq 0$. The first-order central difference method [35] can be employed to acquire the transmission matrix.

$$\mathbf{M_{REG}} = \begin{pmatrix} 1+\frac{i\omega C_0 R_0}{2}g(\tau,Pr) & -\frac{R_0(\tau+1)}{2}f(\tau,Pr) \\ -i\frac{\omega C_0\tau}{\tau-1}ln\tau & \tau \end{pmatrix} \tag{10}$$

where,

$$R_0 = \frac{6\mu_{g,0}l}{Ar_h^2} \tag{11}$$

$$C_0 = \frac{\Phi Al}{P_m} \tag{12}$$

$$f(\tau, Pr) = \frac{2}{Pr+2}\left[\frac{\tau^{Pr+2}-1}{\tau^2-1}\right] \tag{13}$$

$$g(\tau, Pr) = \frac{2}{Pr+2}\left[\frac{\tau^{Pr+2} ln\tau - (\tau^{Pr+2}-1)/(Pr+2)}{(\tau-1)^2}\right] \tag{14}$$

In the resonator, the transfer matrix is presented as follows:

$$\mathbf{M_{RT}} = \begin{pmatrix} cos\left(\frac{\omega l}{a}\right) & -\frac{a\rho_m sin(\omega l/a)}{A} i \\ -\frac{Asin(\omega l/a)}{a\rho_m} i & cos\left(\frac{\omega l}{a}\right) \end{pmatrix} \tag{15}$$

For the whole phase modulation structure section, it consists of two resonators and one cavity. The transfer matrix of this section can be integrated as:

$$\mathbf{M_{GR}} = \mathbf{M_{RT1}}\mathbf{M_{CVT}}\mathbf{M_{RT2}} \tag{16}$$

According to the thermoacoustic network theory [35], the total transfer matrix of the looped single-stage heat-driven thermoacoustic refrigerator, $\mathbf{M_{all}}$, can be given by

$$\mathbf{M_{all}} = \mathbf{M_{AHXe}}\mathbf{M_{REGe}}\mathbf{M_{HHXe}}\mathbf{M_{TBTe}}\mathbf{M_{AHXc}}\mathbf{M_{REGc}}\mathbf{M_{CHXc}}\mathbf{M_{PTc}}\mathbf{M_{GR}} \tag{17}$$

For the n-level looped thermoacoustic system, the transfer matrix, $\mathbf{M_{sub}}$, can be expressed as

$$\mathbf{M_{sub}} = \begin{pmatrix} cos\left(\frac{2\pi}{n}\right) - isin\left(\frac{2\pi}{n}\right) & 0 \\ 0 & cos\left(\frac{2\pi}{n}\right) - isin\left(\frac{2\pi}{n}\right) \end{pmatrix} \tag{18}$$

where n is the number of stages. Therefore, the transfer equation of the thermoacoustic system is:

$$\begin{pmatrix} P_1(x_{out}) \\ U_1(x_{out}) \end{pmatrix} = \mathbf{M_{all}} \begin{pmatrix} P_1(x_{in}) \\ U_1(x_{in}) \end{pmatrix} = \mathbf{M_{sub}} \begin{pmatrix} P_1(x_{in}) \\ U_1(x_{in}) \end{pmatrix} \tag{19}$$

The following equation must be satisfied to acquire a non-zero solution in Eq. (19):

$$\begin{vmatrix} m_{all,11} - m_{sub,11} & m_{all,12} \\ m_{all,21} & m_{all,22} - m_{sub,22} \end{vmatrix} = 0 \tag{20}$$

The onset characteristic parameters ω and τ of the looped single-stage heat-driven thermoacoustic refrigerator can be obtained by solving Eq. (20).

3.2. Time-domain model description

In this work, the steady characteristics of the looped single-stage heat-driven thermoacoustic refrigerator is simulated on the SAGE program [36]. SAGE is widely used in modeling and calculating the parameters of thermoacoustic devices [11,37]. The calculation and optimization of the refrigerator are based on the conservation equations of mass, momentum, and energy in the corresponding gas domain, which are respectively:

$$\frac{\partial \rho A}{\partial t} + \frac{\partial \rho u A}{\partial x} = 0 \tag{21}$$

$$\frac{\partial \rho u A}{\partial t} + \frac{\partial u \rho u A}{\partial x} + \frac{\partial p}{\partial x} A - FA = 0 \tag{22}$$

$$\frac{\partial \rho e \mathrm{A}}{\partial \mathrm{t}} + p\frac{\partial \mathrm{A}}{\partial t} + \frac{\partial}{\partial x}(u\rho eA + upA + q) - Q_w = 0 \tag{23}$$

The source terms F, q and Q_w are calculated as empirical functions which are,

$$F = -(f_D/d_h + K_{los}/l)\rho u|u|/2 \tag{24}$$

$$q = -N_k k_g \frac{\partial T}{\partial x} A \tag{25}$$

$$Q_w = Nu\left(k_g/d_h\right) S_x (T_w - T) \tag{26}$$

Additionally, some parameters used to describe the performance of the system can be viewed in Appendix A.

3.3. Model validations

To simultaneously validate the accuracy of the frequency-domain model (Section 3.1) for calculating the onset characteristics and the time-domain model (Section 3.2) for simulating the steady-state performance in this work, a prototype of a single-unit direct-coupled looped thermoacoustic refrigeration system was constructed. The experimental structure is similar to that of Fig. 1 with only some differences in dimensions that do not affect regularity. Helium was used as the working gas in this series of experiments, and the ambient temperature was determined to be 35 °C.

Fig. 2 shows the comparison between the experimental and calculation results on the onset characteristics including onset heating temperature ($T_{h,onset}$) and onset frequency (f_{onset}). Fig. 3 shows the comparison between the experimental and calculation results on the steady-state system performance including cooling power (Q_c) and Coefficient of Performance (COP). The heating temperature is set at 300 °C and the mean operating pressure is 8 MPa in the steady-state experimental tests. The average discrepancies in onset heating temperature, onset frequency, cooling power, and Coefficient of Performance are 8.5%, 6.8%, 1.1%, and 15.3%, respectively. Therefore, the overall accuracies of the frequency-domain and time-domain models on calculating and simulating the onset characteristics and steady-state system performance can still be considered reliable.

4. Results and discussions

4.1. Onset performances analysis

This section focuses on the effect of an important parameter, mean pressure, on the onset performance for different working gases, since the mean pressure has a direct effect on the transfer matrix as shown in Eqs. (1) and (2). It also straightforwardly affects the gas thermal properties such as gas mean density and penetration depths, which decisively involves in determining the system onset characteristics. Fig. 4 shows the variation of onset temperature difference and onset frequency with the mean pressure for different working gases. For the given pressure, the onset temperature difference with nitrogen systems is the lowest among the four gases. As the mean pressure increases, the onset temperature difference decreases with more sensitivity to the variation at lower mean pressures (≤ 4 MPa). For gas helium, it decreases from 207 K to 93 K when the mean pressure increases from 1 MPa to 4 MPa. Continuing to increase the mean pressure, the onset temperature difference decreases at a slower rate. However, according to Fig. 4 (b), the onset frequency remains almost constant with increasing average pressure for different gases. The onset frequencies of helium, nitrogen, hydrogen, and argon are respectively around 74 Hz, 26 Hz, 95 Hz and 23 Hz. The increase of the mean pressure seems to slightly affect the onset frequency compared to the onset temperature difference as the oscillation frequency is mainly influenced by the structural dimensions and boundary conditions of the system [38].

4.2. Steady characteristics analysis

4.2.1. Cooling performance and exergy losses analysis

Table 2 shows the simulation results of Sage when mean pressure is 10 MPa, ambient temperature is 323 K, heating temperature is 573 K, and cooling temperature is 280 K. The proposed thermoacoustic

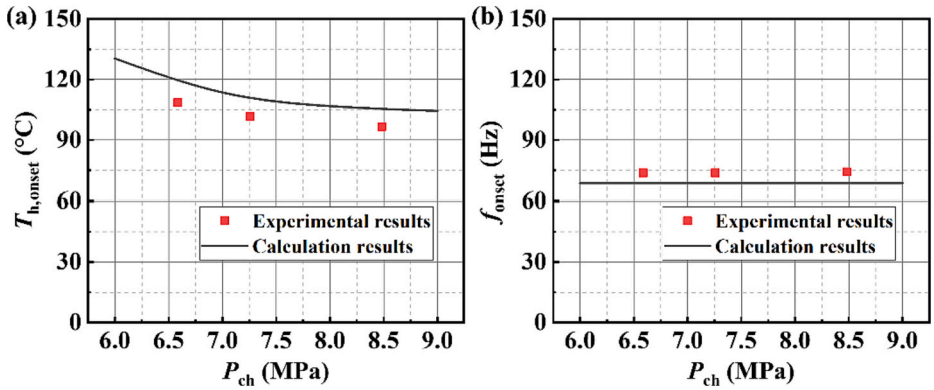

Fig. 2. Comparison of experimental and calculation results on the onset characteristics including (a) onset heating temperature ($T_{h,onset}$) and (b) onset frequency (f_{onset}).

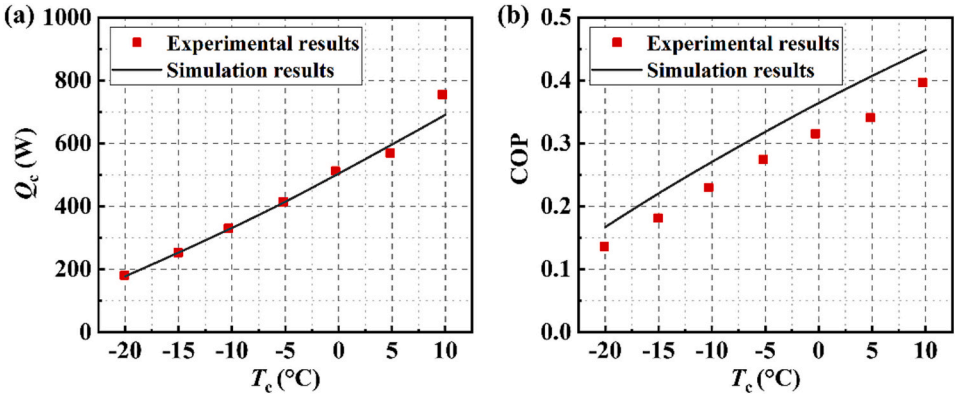

Fig. 3. Comparison of experimental and simulation results on the steady-state system performance including (a) cooling power (Q_c) and (b) Coefficient of Performance (COP).

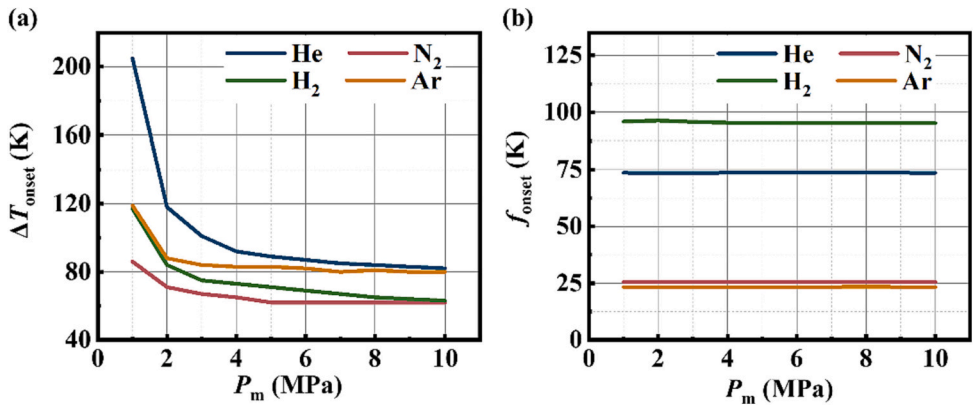

Fig. 4. Effect of the mean pressure on the (a) onset temperature difference and (b) onset frequency for 4 different working gases.

refrigerator obtained a cooling power of 6.43 kW, an overall Coefficient of Performance (COP) of 0.439, and a relative Carnot efficiency of 15.4%. Notably, 10 MPa is feasible for the present closed system, which has been verified in similar experiments [14]. However, the practical long-term stable operation may necessitate certain requirements regarding the system's pressure capacity and sealing ability.

Fig. 5 shows the exergy losses of the different components of the proposed refrigerator, which allows a direct estimation of the work capacity reduction in each component induced by the irreversible process. In the gas domain, both the conduction of heat across finite temperature differences and the irreversible flow processes generate entropy, which is used to calculate the exergy losses by multiplying the normalization temperature (T_0) [39]. The losses are generally classified as the flow friction losses (AE_{fric}), the non-ideal heat transfer losses between the gas and the solid (AE_{Qw}), the axial heat flow losses (AE_{Qx}), and the loss discrepancy, which are respectively showed as Eqs. (33)–(35) [39]. In the proposed refrigerator, the three components with the largest losses are, in order, the RTs (1291 W), the REGe (1183 W), and the REGc (803 W). In this case, the acoustic impedance is larger in the regenerators, so the non-ideal heat transfer losses account for most of the exergy losses (i.e., 72.3% for the REGe and 42.4% for the REGc). And in the gas resonator unit, it is the large tube length that causes the large flow friction

Table 2
Simulation results for the specific condition.

Symbol	Parameter	Value
P_m	Mean pressure (MPa)	10
P_r	Pressure ratio at inlet of engine stage	1.09
T_h	Heating temperature (K)	573
T_c	Cooling temperature (K)	280
T_a	Ambient temperature (K)	323
f	Working frequency (Hz)	74.9
Q_h	Heating power (kW)	14.7
Q_c	Cooling power (kW)	6.43
ε_e	The capacity of the engine stage to amplify acoustic power	0.51
η_e	The capacity of the engine stage to convert acoustic power to heat	0.26
ε_c	The capacity of the refrigerator stage to utilize acoustic power	0.29
η_c	Coefficient of Performance of the refrigerator stage	2.5
COP	Coefficient of Performance of the system	0.439
η	Relative Carnot efficiency of the system	15.4%

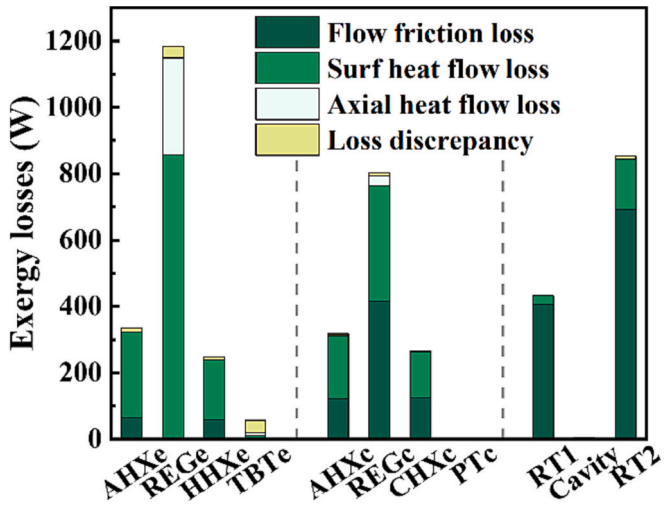

Fig. 5. Exergy losses in different components. AHX is the ambient-temperature heat exchanger, REG is the regenerator, HHX is the high-temperature heat exchangers, TBT is the thermal buffer tube, CHX is the low-temperature heat exchanger, PT is the pulse tube, and RT is the resonant-tube. *e* is for the engine, and *c* is for the cooler.

loss (i.e., 93.7% for the RT_1 and 81.3% for the RT_2).

$$AE_{fric} = -T_0 \times \oint_{dt}\int_{dx} \frac{uAF}{T} \tag{33}$$

$$AE_{Qw} = -T_0 \times \oint_{dt}\int_{dv} \frac{q_w \bullet \nabla T_w}{T^2} \tag{34}$$

$$AE_{Qx} = -T_0 \times \oint_{dt}\int_{dv} \frac{q_x \bullet \nabla T_x}{T^2} \tag{35}$$

4.2.2. Axial distributions of key parameters

The axial distributions of key parameters enable an accurate assessment of the thermoacoustic characteristics and are shown in Fig. 6. The axial position is from the inlet of AHXe to the outlet of RT_2 for a loop. Fig. 6 (a-c) shows the variations of the key parameters including the amplitude and phase of the pressure and volume flow rate waves, the phase difference between the two, and the acoustic power. As shown in Fig. 6 (c), the phase difference of the pressure and volume flow rate waves (θ_{P-U}) increases from −39.6° to 37.3° in the thermoacoustic core unit, decreases from 37.3° to −9.8° in RT_1, increases again from −9.8° to 18.7° in the cavity, and then varies from 18.7° to −46.2° along with a trend of decreasing-increasing-decreasing. The distribution of the phase difference reveals that the cavity structure anchors a velocity node at

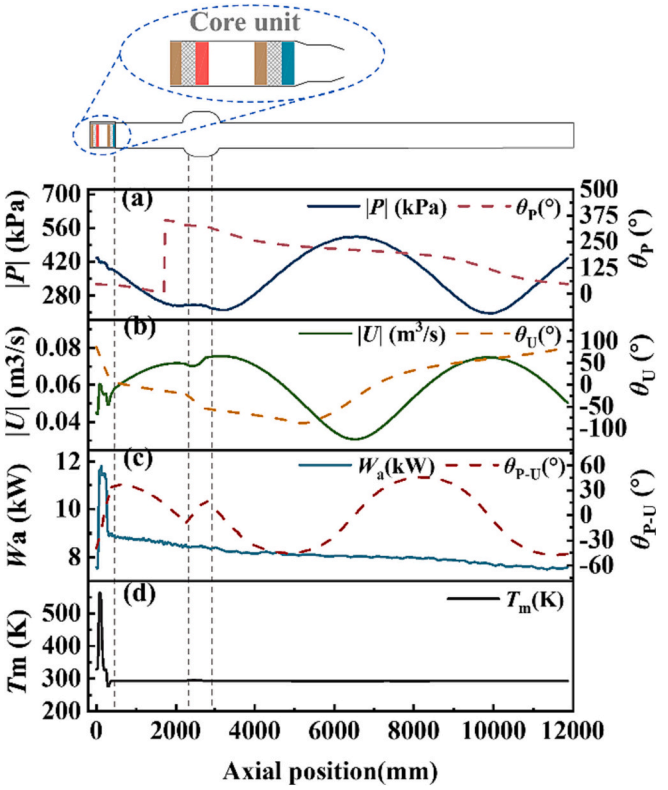

Fig. 6. Axial distributions of the (a) amplitude and phase of the pressure wave (b) amplitude and phase of the volume flow rate (c) acoustic power and phase difference between the pressure wave and volume flow rate (d) mean gas temperature, in the looped single-stage system with one cavity. The P_m is 10 MPa, T_a is 323 K, T_h is 573 K and T_c is 280 K.

about one-quarter wavelength of the system, thus establishing a traveling-wave dominated acoustic field within the regenerators, which enables efficient energy conversion in a thermoacoustic system [40]. For the acoustic power distribution, initially, 7574 W of acoustic power is generated and then amplified to 11,610 W in the engine stage. After the utilization of the cooler stage, the acoustic power is reduced to 6033 W. Approximately 1314 W of acoustic power is dissipated in the gas resonator unit. Finally, about 7573 W of acoustic power is recycled and participates in the next thermodynamic cycle.

Fig. 6 (d) shows the distribution of mean gas temperature along the loop. The working gas is heated from 333 K to 559 K in the REGe with a 5.65 K/mm of the mean temperature gradient, and then drops from 560 K to 328 K in the TBTe. The average gas temperature is reduced to 277 K under the cooling of the REGc. Finally, the gas temperature is restored to the proposed atmospheric temperature (293 K) in the pulse tube and remains largely constant in the subsequent structure.

4.2.3. Analyzing the cooling performances under different working conditions

In the case of practical cooling applications, the actual operating conditions may vary. For example, the heating temperature may vary with the heat source conditions, especially in the case of waste heat utilization; the ambient temperature may also vary with factors such as weather changes; and there are usually variable cooling temperature requirements as well. It is therefore necessary to explore the cooling performance under different working conditions, which is shown in Fig. 7.

A decrease in ambient temperature as well as an increase in heating temperature and cooling temperature would generally lead to an increase in cooling power (Q_c) and Coefficient of Performance (COP) of the system. Fig. 7 (a) and (b) show the effect of heating temperature on

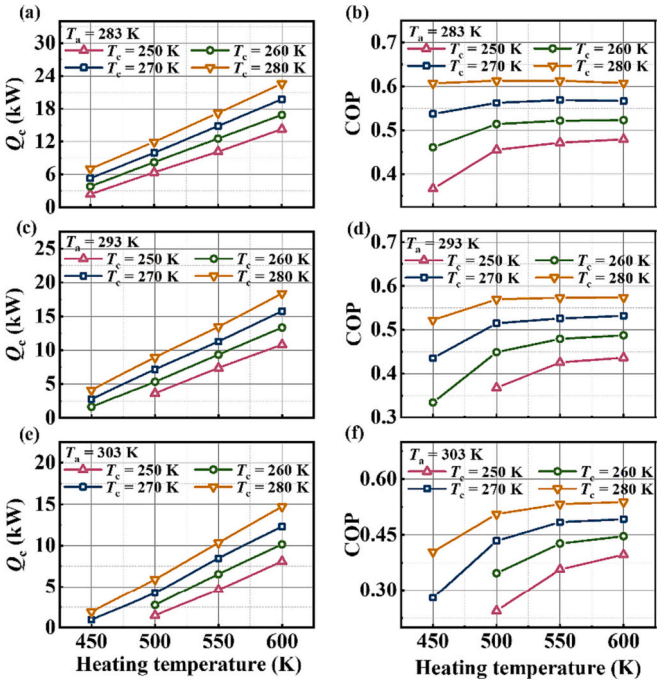

Fig. 7. Effect of the heating temperature on cooling power and coefficient of performance of the system with ambient temperature and cooling temperature changes. P_m is 10 MPa, T_a is 283 K in (a) and (b), 293 K in (c) and (d), and 303 K in (e) and (f).

cooling performance at different cooling temperatures when the ambient temperature is fixed at 283 K. The results show that the system can achieve an ultra-low cooling temperature while maintaining good refrigeration performance. Even at a heating temperature of 450 K and a cooling temperature of 250 K, a cooling power of 2.38 kW and a COP of 0.37 can be achieved.

Fig. 7 (c) and (d) present the cooling performance of the system at relatively mild temperatures, i.e., an ambient temperature of 293 K. The cooling performance of the system remains relatively good in this temperature range, achieving a cooling power of 13.46 kW and a COP of 0.57 at a heating temperature of 550 K and a cooling temperature of 280 K.

Fig. 7 (e) and (f) show the cooling performance of the system at relatively high ambient temperatures, i.e., at an ambient temperature of 303 K. The performance of the system is significantly affected at this ambient temperature. Particularly when the heating temperature is 450 K, the refrigerator is no longer able to achieve cooling temperatures of 250 K and 260 K. When the cooling temperature is increased to 280 K, a cooling power of 14.71 kW and a COP of 0.54 can be achieved at a heating temperature of 600 K.

Notably, at different ambient temperatures, there exists a maximum value of COP when the heating temperature rises, although the cooling power rises as the increasing heating temperature, which means that the cooling efficiency is limited by temperature. A simple explanation is that in a looped direct-coupled structure, there is a correspondence between the conversion of energy and the temperature (especially the temperature ratio) of the core unit. Therefore, at a given ambient temperature and cooling temperature, there is also a corresponding heating temperature that maximizes cooling efficiency. As the temperature continues to increase, although the cooling power is increased, the excess energy cannot be efficiently converted due to the limitation of the temperature ratio of the cooler unit.

4.2.4. *Effect of adding different gases to the working medium*

The working gas is the essential for energy conversion in thermoacoustic devices. The molecular weight of helium is only 4. Its sound speed is high, and the system operating frequency is relatively high. Adding a certain percentage of other working gases to helium increases the molecular weight and reduces the speed of sound, thus reducing the system frequency.

This subsection focuses on the addition of different proportions of other gases to the original working gas of helium and investigates the effect of the added gases on the system performance. Three different working fluids, argon, carbon dioxide, and xenon, are selected in this study, and their physical performance parameters at specific operating conditions are presented in Table 3.

Fig. 8 (a) and (b) show that the cooling power of the system tends to decrease as the proportion of the working gases increases due to the difference in the heat transfer properties of the mixed gases. The cooling power decreases the fastest when xenon is added among the three, followed by carbon dioxide, and the slowest when argon is added. The COP tends to increase and then decrease when the percentage of xenon added increases, while for carbon dioxide and argon it tends to decrease. When 20% of argon is added to helium, the cooling power was reduced from 6433 W to 4016 W and the COP was reduced from 0.439 to 0.412, respectively.

Fig. 8 (c) shows the effect of adding different proportions of other working gases to helium on the operating frequency of the system. The system frequency decreases significantly when the proportion increases. The largest reduction is observed with the addition of xenon, followed by carbon dioxide, and the smallest with the addition of argon. When 20% of xenon is added, the system frequency was reduced from 74.9 Hz to 27.6 Hz, a reduction of about 63.2%.

The simulation results show that the addition of a certain percentage of other working gases to helium can effectively reduce the system frequency. In particular, the proper addition of xenon can significantly reduce the system frequency without noticeable reduction in COP.

4.2.5. *Effect of the cavity position with varied cavity volumes*

The analysis of the axial distribution of the key parameters in previous section indicates that the cavity structure plays an important phase-matching role. This section focuses on the influence of two important parameters of the cavity structure - dimension and position in the system - on the system cooling performance.

The first is about the position of the cavity in the system. The cavity position can be defined as $l_1 / (l_1 + l_2)$, where l_1 and l_2 are the lengths of RT_1 and RT_2, respectively. Controlling the value of $(l_1 + l_2)$ constant, by changing l_1 and l_2, the position of the cavity in the system can be adjusted and the effect on the cooling performance of the system can be explored. The second is about the dimensions, which mainly refers to the volume of the cavity. Since changing the length of the cavity affects the overall length of the system, which in turn has effect on the working frequency. This study selects to control the volume change of the cavity by altering the diameter of the cavity in order to control the system frequency change as little as possible. Fig. 9 shows the schematic of the two parameter changes mentioned above.

Fig. 10 shows the effect of cavity position and cavity volume on the cooling power and COP for a given condition when P_m is 10 MPa, T_a is 323 K, T_h is 573 K and T_c is 280 K. The results for the key values are the

Table 3
Physical performance parameters of the corresponding working fluids under specific operating conditions when P_m is 10 MPa, T_a is 323 K, T_h is 573 K and T_c is 280 K.

Working fluids	c_p (J kg^{-1} K^{-1})	k ($\times 10^{-3}$ W m^{-1} K^{-1})	μ ($\times 10^{-6}$ Pa·s)	Prandtl number
He	5194.1	170.24	21.268	0.649
Ar	623.3	22.876	26.676	0.727
CO_2	5888.4	52.824	28.508	3.178
Xe	998.8	21.716	54.45	2.504

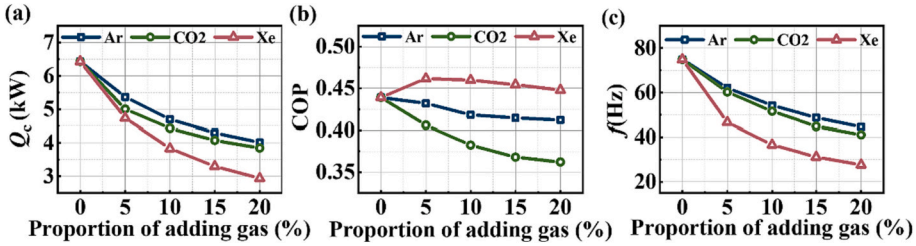

Fig. 8. Effect of adding gas proportion on (a) cooling power (b) coefficient of performance (c) working frequency, in the looped single-stage system with one cavity. P_m is 10 MPa, T_a is 323 K, T_h is 573 K and T_c is 280 K.

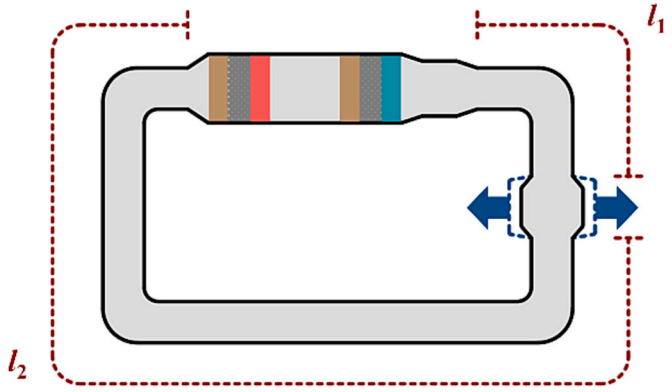

Fig. 9. Schematic of the proposed thermoacoustic refrigerator with cavity position and volume changes. l_1 and l_2 respectively represent the lengths of RT_1 and RT_2. The blue arrows mean the diameter of the cavity is adjustable. (For interpretation of the references to colour in this figure legend, the reader is referred to the web version of this article.)

results of the sage calculations, and the intermediate values are the results of the interpolated grid, where grid density is 15 × 15. It can be noted that both can significantly affect the system performance, especially when the cavity position is varied, the magnitude of cooling performance change is large. This is not something to be delighted about, as it means that a high precision is required for cavity installation in engineering applications. Additionally, the cooling power achieved a maximum value of 6.37 kW at 16.5% in the cavity position and a cavity volume of 6.1 × 10^6 mm^3. The COP achieved a maximum value of 0.47 at 17.9% in the cavity position and a cavity volume of 6.6 × 10^6 mm^3. The fact that these two important parameters reach their maximum values at different points provides important insights into the trade-off decisions between cooling power and cooling efficiency by changing the position and volume of the cavity.

4.3. Further investigations on the multi-cavity configurations

The above research focuses on the single-stage thermoacoustic refrigerator with only one cavity. Considering the importance of cavity structure for single-stage thermoacoustic refrigerators, this section examines the changes in system performance when the number of cavities is increased to 2 and 3. Fig. 11 (a-c) show schematics of the looped single-stage heat-driven thermoacoustic refrigerators with one, two, and three cavities, respectively, for intuitive comparison. They are optimized with the same thermoacoustic core unit parameters, cavity size, and resonant-tube diameter as the single-cavity structure. The overall dimensions of the three structures were also controlled to be similar during optimization to ensure no major differences in system frequencies. The differences lie in the number of cavities, the number of resonant-tube segments, and the length of each resonant-tube. Table 4 presents the optimized dimensions of the resonator parts in the system of the structures with 1, 2, and 3 cavities respectively.

Similar numerical simulations are performed for the multi-cavity structures under specific operating conditions when P_m is 10 MPa, T_a is 323 K, T_h is 573 K and T_c is 280 K, and the calculated results are presented in Table 5. The results show that the pressure ratio at the inlet of the engine stage decreases when the number of cavities increases, under similar operating conditions and working frequency. The heating power and cooling power show a decreasing trend, while the COP and relative Carnot efficiency of the system are not significantly affected by the number of cavities. The above simulation results suggest that the resonator with a single cavity is better matched to the thermoacoustic core unit for these specific parameters. In addition, the optimization of

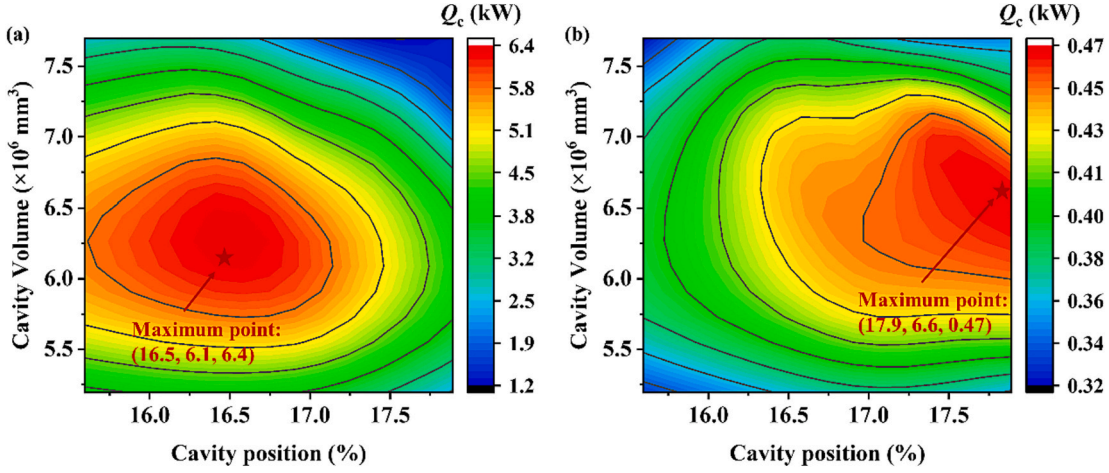

Fig. 10. Effect of cavity position (l_1 / (l_1 + l_2)) and cavity volume on (a) cooling power (b) coefficient of performance, in the looped single-stage system with one cavity. P_m is 10 MPa, T_a is 323 K, T_h is 573 K and T_c is 280 K.

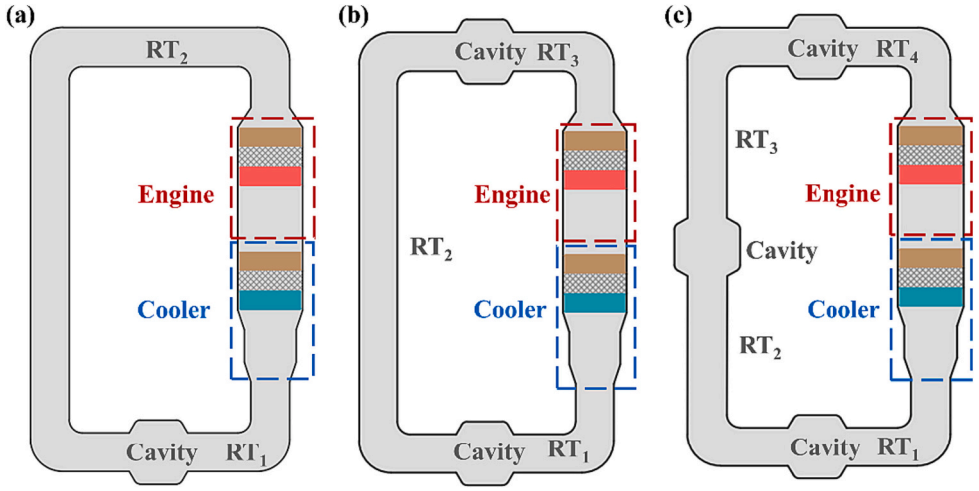

Fig. 11. Schematics of looped single-stage heat-driven thermoacoustic refrigerators with (a) one cavity, (b) two cavities, and (c) three cavities.

Table 4
Dimensions of the resonator parts in system of the structure with 1, 2 and 3 cavities respectively. These three structures have the same cavity dimensions, differing only in the number of cavities.

Number of cavities	Parts	Diameter (mm)	Length (mm)
1	Cavity	126	500
	RT_1	55	1800
	RT_2	55	9100
2	Cavity	126	500
	RT_1	55	2700
	RT_2	55	3100
	RT_3	55	3400
3	Cavity	126	500
	RT_1	55	2400
	RT_2	55	2150
	RT_3	55	1550
	RT_4	55	2400

Table 5
A comparison of the simulation results in systems with 1, 2 and 3 cavities respectively for the case when P_m is 10 MPa, T_a is 323 K, T_h is 573 K and T_c is 280 K.

Number of cavities	1	2	3
f (Hz)	74.87	74.67	74.5
pr	1.091	1.084	1.08
Q_h (kW)	14.65	13.4	11.32
Q_c (kW)	6.433	5.71	4.856
COP	0.439	0.426	0.429
η	15.45%	15%	15.1%

the whole system for this single-cavity structure has reached a relatively good value. There may be potential for further exploration of the parameters of the thermoacoustic core unit that are better matched to each of the multi-cavity structures.

Fig. 12 shows the axial distributions of the phase difference between the pressure wave and volume flow rate in multi-cavity systems. The x-axis begins equally at the inlet of the engine unit and ends at the outlet of the last resonant-tube. Overall, the phase difference increases in the thermoacoustic core unit, decreases in the resonator sections, and increases in the cavity sections, except for the RT_2 in the single-cavity structure. The results show that the traveling-wave acoustic fields dominate the thermoacoustic core unit of the double-cavity structure (phase difference from −39.1° to 34.1°) as well as the triple-cavity structure (phase difference from −41.8° to 37.1°), which means that three proposed systems satisfy the conditions for efficient energy

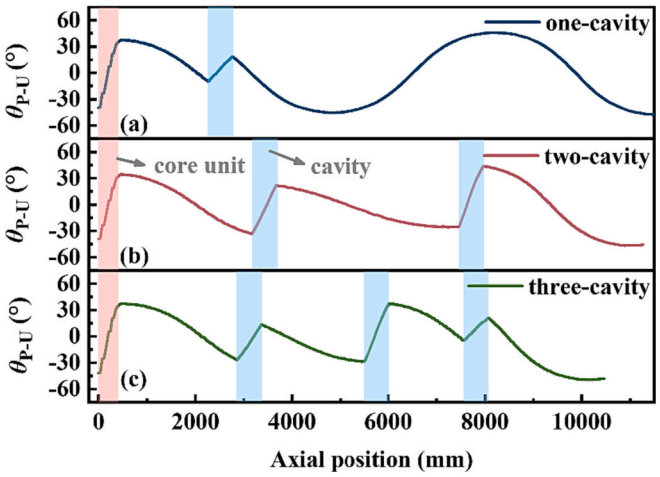

Fig. 12. Predicted axial distributions of the phase difference between the pressure wave and volume flow rate in (a) single-cavity system (b) double-cavity system (c) triple-cavity system. The red sections represent the thermoacoustic core unit and the blue sections represent the cavity. P_m is 10 MPa, T_a is 323 K, T_h is 573 K and T_c is 280 K. (For interpretation of the references to colour in this figure legend, the reader is referred to the web version of this article.)

conversion in thermoacoustic systems, since the establishment of the traveling-wave acoustic fields, i.e., the in-phase relationship between P_1 and U_1, across the regenerators .

Onset characteristics are equally studied for the multi-cavity structures. Fig. 13 (a) and (b) shows the variation of onset temperature difference and onset frequency with the cavity number. The results show that the number of cavities does not have a simple positive correlation effect on the onset temperature difference. For different gases, the single-cavity structure has the lowest onset temperature, the double-cavity structure has the highest onset temperature, and the three-cavity structure lies in between. In contrast, the onset frequencies of helium, nitrogen, hydrogen, and argon are respectively around 73 Hz, 26 Hz, 95 Hz and 23 Hz, which are not significantly affected with the cavity numbers.

5. Comparison with the proposed heat-driven cooling technologies

To explore the potential of the proposed heat-driven thermoacoustic

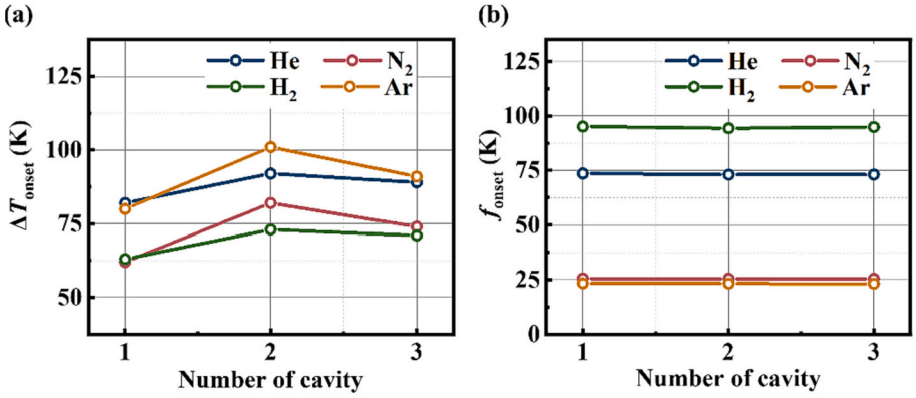

Fig. 13. Effect of the cavity number on the (a) onset temperature difference and (b) onset frequency for different working gases.

refrigerator for domestic cooling applications, this section investigates other typical heat-driven refrigeration technologies currently under development, namely absorption, adsorption, ejector-based, and desiccant-based refrigerators, and provides a brief comparison with the proposed system. Table 6 and Fig. 14 illustrate the comparison with existing heat-driven cooling technologies for domestic applications. Each heat-driven cooling technology has its own optimal working conditions, and these conditions can vary significantly, resulting in different cooling levels for diverse practical application scenarios. Due to its unique alternating flow characteristics, the heat-driven thermoacoustic refrigeration system can realize different levels of cooling power depending on the pressure, thus adapting to various application scenarios. Meanwhile, the thermoacoustic refrigerator uses helium as the working gas which can still work well when the refrigeration temperature cannot go below 0 °C, providing a good complement to the current heat-driven refrigeration technology.

It is important to emphasize, however, that since the different systems are not individually suited to the same operating conditions, including temperature, pressure, and working medium, this chapter does not attempt to identify the most superior heat-driven refrigeration system, but rather to provide a reference for the variability between the different technologies. Heat-driven thermoacoustic refrigeration technology shows a comparable cooling performance with existing heat-driven cooling technologies and has good prospects for application in the field of domestic refrigeration.

6. Conclusions

The present work conducted detailed numerical investigations on a looped single-stage heat-driven thermoacoustic refrigerator for domestic cooling applications. The proposed system is distinguished from previous studies by its inclusion of only one thermoacoustic core, the direct coupling of the cooler unit to the engine unit, and the introduction of cavity features. We first examined the onset characteristics based on the transfer matrix method in frequency domain, and then investigated the steady-state performance by using SAGE program in time domain. Further comparisons were made with the multi-cavity structures and other existing heat-driven refrigeration systems. The key findings are summarized as follows:

(1) The increasing mean pressure and the nitrogen gas selection play a critical but favorable role in reducing the onset temperature difference. A 62 K onset temperature difference is observed in the present system with the usage of 10 MPa nitrogen, which is more favorable for the utilization of lower grade thermal energy.
(2) The proposed refrigerator design can achieve a COP of 0.24–0.61 at the cooling temperatures of −23-7 °C. Depending on the cooling objective, such as air conditioning, refrigeration, and refrigerator freezing, the cooling temperature can be set differently. The parameters such as operating pressure, heating temperature, ambient temperature can be adjusted to make the proposed system achieve the optimum operating conditions. Future efforts to reduce the exergy loss of resonators can further improve the practical applications potential in the domestic cooling sectors.
(3) The system frequency can be significantly reduced by replacing or adding higher molecular mass gases, which might provide ideas in engineering issues such as reducing working mass costs, vibration damping, or downsizing the system. Meanwhile, mixing the appropriate proportion of high-efficiency work gases, such as xenon, can improve the cooling performance of the system.
(4) The single-cavity structure outperforms the multi-cavity structures in terms of cooling performances and onset characteristics as revealed in this work. Further research is needed for the cavity structure to explore its effect on the looped thermoacoustic system.
(5) Our proposed heat-driven thermoacoustic refrigerator has a comparable cooling performance with the existing typical heat-driven cooling technologies in the room temperature range. The present results reveal that the heat-driven thermoacoustic refrigeration technology has good prospects for practical applications in the field of domestic refrigeration.

Table 6
Comparison with existing heat-driven cooling technologies for domestic applications. T_a is fixed at 30 °C for the proposed thermoacoustic refrigerator.

Type	T_h/°C	T_c/°C	Q_c/kW	COP	Medium
This work	300	0–25	1.28–16.2	0.43–0.63	He
Absorption [41–50]	79–115	7–26	2.68–40	0.53–0.7	H_2O/Ammonia; LiBr/H_2O
Adsorption [51–60]	79–200	9–26.3	3.98–42.8	0.37–0.65	silica gel/H_2O; zeolite NaX/H_2O
Ejector [61–65]	70–200	5–12	2.5–10.5	0.39–0.55	R134a et al.
Desiccant [66–70]	65–100	10–20	3–25.6	0.25–0.52	solid or liquid

Although this work suggests the promising prospect of the heat-driven thermoacoustic refrigeration systems for medium/low-grade heat utilization, it is crucial to acknowledge their current early stages of laboratory research. Consideration of engineering issues and further research will be necessary for these systems to be deemed practical for real-world civilian applications.

CRediT authorship contribution statement

Yiwei Hu: Writing – original draft, Validation, Software,

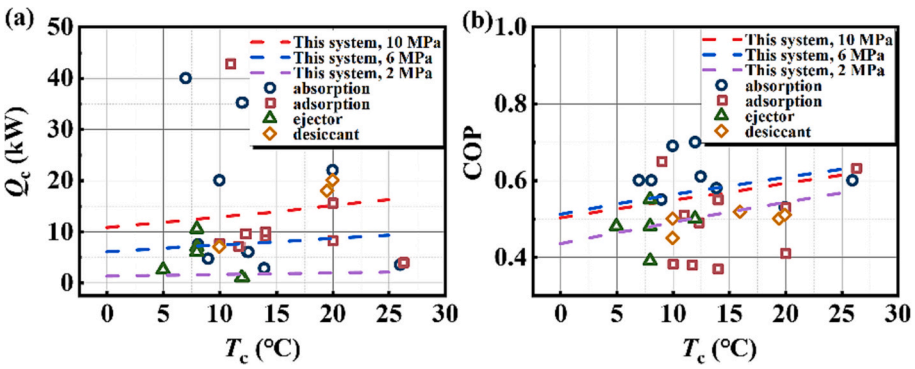

Fig. 14. Comparisons on Q_c and COP between the proposed system and several existing heat-driven cooling technologies for domestic applications.

Methodology, Investigation. **Jingyuan Xu:** Writing – review & editing, Visualization, Supervision, Methodology, Formal analysis, Conceptualization. **Dan Zhao:** Writing – review & editing, Methodology, Investigation. **Rui Yang:** Writing – review & editing, Investigation. **Jianying Hu:** Writing – review & editing, Methodology. **Ercang Luo:** Writing – review & editing, Supervision, Project administration, Funding acquisition, Conceptualization.

Declaration of competing interest

The authors declare that they have no known competing financial interests or personal relationships that could have appeared to influence the work reported in this paper.

Data availability

Data will be made available on request.

Acknowledgments

This research was financially supported by the National Natural Science Foundation of China (Grant No. 51876213 and No. 51976230), Strategic Priority Research Programme, CAS (No. XDA21080300), and the Open Project of CAS Laboratory of Cryogenics, No. CRYO202214. D. Z is financially supported by University of Canterbury with the award No. 452DISDZ.

Appendix A. The capacity of the engine stage to amplify acoustic power can be defined as

$$\varepsilon_e = \frac{\Delta W_e}{W_{ein}} \tag{A1}$$

where ΔW_e is the acoustic power difference between the export and import of the thermoacoustic engine, W_{ein} is the import acoustic power of the engine.

The capacity of the engine stage to convert acoustic power to heat can be defined as

$$\eta_e = \frac{\Delta W_e}{Q_h} \tag{A2}$$

where Q_h is the heat input at the HHXe.

The capacity of the refrigerator stage to utilize acoustic power can be defined as

$$\varepsilon_c = \frac{\Delta W_c}{W_{cin}} \tag{A3}$$

where ΔW_c is the acoustic power difference between the export and import of the thermoacoustic cooler, W_{cin} is the import acoustic power of the cooler.

The coefficient of performance of the refrigerator stage is

$$\eta_c = \frac{Q_c}{\Delta W_c} \tag{A4}$$

where Q_c is the heat absorption at the CHXc.

The coefficient of performance of the system can be expressed as

$$COP = \frac{Q_c}{Q_h} \tag{A5}$$

Eq. (A6) gives the relative Carnot efficiency of the system,

$$\eta_c = \frac{Q_c\left(\frac{T_a}{T_c} - 1\right)}{Q_h\left(1 - \frac{T_a}{T_h}\right)} \tag{A6}$$

where T_a, T_h and T_c are ambient temperature, heating temperature and cooling temperature respectively.

References

[1] Sarbu I, Sebarchievici C. Review of solar refrigeration and cooling systems. Energ Buildings 2013;67:286–97.
[2] Oktay Z, Aslan A. Geothermal district heating in Turkey: the Gonen case study. Geothermics 2007;36:167–82.
[3] Yang S, Shao X-F, Luo J-H, Baghaei Oskouei S, Bayer Ö, Fan L-W. A novel cascade latent heat thermal energy storage system consisting of erythritol and paraffin wax for deep recovery of medium-temperature industrial waste heat. Energy 2023;265:126359.
[4] Johnson I, Choate WT, Davidson A. Waste heat recovery. United States: Technology and Opportunities in U.S. Industry; 2008.
[5] Kharseh M, Altorkmany L, Nordell B. Global warming's impact on the performance of GSHP. Renew Energy 2011;36:1485–91.
[6] Seyboth K, Beurskens L, Langniss O, Sims REH. Recognising the potential for renewable energy heating and cooling. Energy Policy 2008;36:2460–3.
[7] Wang X, Yu J, Zhou M, Lv X. Comparative studies of ejector-expansion vapor compression refrigeration cycles for applications in domestic refrigerator-freezers. Energy 2014;70:635–42.
[8] Hu Y, Luo K, Zhao D, Wu Z, Yang Y, Luo E, et al. Thermoacoustic heat pump utilizing medium/low-grade heat sources for domestic building heating. Energy Built Environ 2024;5:628–39.
[9] Yang Y, Chi J, Wu Z, Yang R, Xu J, Zhang L, et al. A heat-driven combined cooling and heating system based on thermoacoustic technology. Appl Phys Lett 2022;120:223902.
[10] Hu Y, Wang X, Wu Z, Zhang L, Chen G, Xu J, et al. A thermoacoustic cooler with a bypass expansion for distributed-temperature heat loads. Appl Phys Lett 2022;121:203905.
[11] Xu J, Hu J, Zhang L, Luo E. A looped three-stage cascade traveling-wave thermoacoustically-driven cryocooler. Energy 2016;112:804–9.
[12] Chang D, Hu J, Sun Y, Zhang L, Chen Y, Luo E. Numerical investigation on key parameters of a double-acting free piston Stirling generator. Energy 2023;278:128003.
[13] Guo L, Zhao D, Becker S. Temperature difference and stack plate spacing effects on thermodynamic performances of standing-wave Thermoacoustic engines driven by cryogenic liquids and waste heat. J Therm Sci 2022;31:1434–51.
[14] Chi J, Yang Y, Wu Z, Yang R, Li P, Xu J, et al. Numerical and experimental investigation on a novel heat-driven thermoacoustic refrigerator for room-temperature cooling. Appl Therm Eng 2023;218:119330.
[15] Wang H, Zhang L, Yu G, Hu J, Luo E, Ma Y, et al. A looped heat-driven thermoacoustic refrigeration system with direct-coupling configuration for room temperature cooling. Sci Bull 2019;64:8–10.
[16] Zhu S, Yu G, Ma Y, Cheng Y, Wang Y, Yu S, et al. A free-piston Stirling generator integrated with a parabolic trough collector for thermal-to-electric conversion of solar energy. Appl Energy 2019;242:1248–58.
[17] Radebaugh R, Mcdermott KM, Swift GW, Martin RA. Development of a thermoacoustically driven orifice pulse tube refrigerator. In: Proceedings of the interagency meeting on cryocoolers. Plymouth, MA; 1990. p. 205–20.
[18] Backhaus S, Swift G, W.. A thermoacoustic Stirling heat engine. Nature 1999;399:335–8.
[19] Dai W, Luo E, Zhang Y, Ling H. Detailed study of a traveling wave thermoacoustic refrigerator driven by a traveling wave thermoacoustic engine. J Acoust Soc Am 2006;119:2686–92.
[20] Luo E, Wei D, Yong Z, Hong L. Thermoacoustically driven refrigerator with double thermoacoustic-Stirling cycles. Appl Phys Lett 2006;88:848.
[21] Li S. Study on traveling-wave Thermoacoustic engine, refrigerator and the coupling law in between. The Key Laboratory of Cryogenics, Technical Institute of Physics and Chemistry, Chinese Academy of Science (Beijing); 2009.
[22] Esmatullah Maiwand, Sharify Shinya, Hasegawa.. Traveling-wave thermoacoustic refrigerator driven by a multistage traveling-wave thermoacoustic engine - ScienceDirect. Appl Therm Eng 2017;113:791–5.
[23] Yazaki T, Biwa T, Tominaga A. A pistonless Stirling cooler. Appl Phys Lett 2002;80:157–9.
[24] Blok KD. Low operating temperature integral thermo acoustic devices for solar cooling and waste heat recovery. J Acoust Soc Am 2008;123:3541.
[25] Blok KD. Multi-stage traveling wave thermoacoustics in practice. In: Proc of the 19th international congress on sound and vibration Vilnius. Lithuania: International Institute of Acoustics and Vibration and Vilnius University; 2012. p. 1–8.
[26] Ding X, Chen Z, Kang H, Zhang L. Research on thermoacoustic refrigeration system driven by waste heat of industrial buildings. Sustain Energy Technol 2023;55:102971.
[27] Jin T, Yang R, Wang Y, Liu Y, Feng Y. Phase adjustment analysis and performance of a looped thermoacoustic prime mover with compliance/resistance tube. Appl Energy 2016;183:290–8.
[28] Saechan P, Jaworski AJ. Thermoacoustic cooler to meet medical storage needs of rural communities in developing countries. Therm Sci Eng Progr 2018;7:164–75.
[29] Farikhah I. The effect of mean pressure on the performance of a single-stage heat-driven thermoacoustic cooler. Int J Low-Carbon Technol 2020;15:471–6.
[30] Xu J, Luo E, Hochgreb S. Study on a heat-driven thermoacoustic refrigerator for low-grade heat recovery. Appl Energy 2020;271:115167.
[31] Jin T, Yang R, Wang Y, Feng Y, Tang K. Acoustic field characteristics and performance analysis of a looped travelling-wave thermoacoustic refrigerator. Energ Convers Manage 2016;123:243–51.
[32] Wang H. Theoretical and experimental investigation on a double-traveling looped heat-driven thermoacoustic refrigerator for room temperature cooling. The Key Laboratory of Cryogenics, Technical Institute of Physics and Chemistry, Chinese Academy of Science (Beijing); 2020.
[33] Swift W Gregory. Thermoacoustic engines. J Acoust Soc Am 1988;4:1809.
[34] Swift GW. Thermoacoustics: A unifying perspective for some engines and refrigerators. 2 ed. Springer Cham; 2001.
[35] Raspet R, Brewster J, Bass HE. A new approximation method for thermoacoustic calculations. J Acoust Soc Am 1998;103:2395–402.
[36] Gedeon D. SAGE - Object-oriented software for cryocooler design. In: 8th international cryocooler conference (Cryocoolers 8), Vail, Colorado; 1994. p. 281–92.
[37] Xu J, Hu J, Luo E, Zhang L, Dai W. A cascade-looped thermoacoustic driven cryocooler with different-diameter resonance tubes. Part I: theoretical analysis of thermodynamic performance and characteristics. Energy 2019;181:943–53.
[38] Zhang X, Chang J. Onset and steady-operation features of low temperature differential multi-stage travelling wave thermoacoustic engines for low grade energy utilization. Energy Convers Manag 2015;105:810–6.
[39] Gedeon D. Sage user's guide - Stirling, pulse-tube and low-T cooler model classes. v12 ed. 2021 Available from: http://sageofathens.com/Documents/documents.php.
[40] Zhang L, Hu J, Wu Z, Luo E, Xu J, Bi T. A 1 kW-class multi-stage heat-driven thermoacoustic cryocooler system operating at liquefied natural gas temperature range107; 2015. 033905.
[41] Agyenim F, Knight I, Rhodes M. Design and experimental testing of the performance of an outdoor LiBr/H2O solar thermal absorption cooling system with a cold store. Sol Energy 2010;84:735–44.
[42] Asim M, Dewsbury J, Kanan S. TRNSYS simulation of a solar cooling system for the hot climate of Pakistan. In: 4th international conference on solar heating and cooling for buildings and industry (SHC), Istanbul, TURKEY; 2015. p. 702–6.
[43] Chen JF, Dai YJ, Wang RZ. Experimental and analytical study on an air-cooled single effect LiBr-H2O absorption chiller driven by evacuated glass tube solar collector for cooling application in residential buildings. Sol Energy 2017;151:110–8.
[44] Christopher SS, Santosh R, Vikram MP, Prabakaran R, Thakur AK, Xu HJ. Optimization of a solar water heating system for vapor absorption refrigeration system. Environ Prog Sustain Energy 2021;40.
[45] Ibrahim NI, Al-Sulaiman FA, Ani FN. Performance characteristics of a solar driven lithium bromide-water absorption chiller integrated with absorption energy storage. Energ Convers Manage 2017;150:188–200.
[46] Li ZF, Sumathy K. Experimental studies on a solar powered air conditioning system with partitioned hot water storage tank. Sol Energy 2001;71:285–97.
[47] Rahman A, Abas N, Dilshad S, Saleem MS. A case study of thermal analysis of a solar assisted absorption air-conditioning system using R-410A for domestic applications. Case Stud Therm Eng 2021;26:101008.
[48] Rosiek S, Batlles FJ. Integration of the solar thermal energy in the construction: analysis of the solar-assisted air-conditioning system installed in CIESOL building. Renew Energy 2009;34:1423–31.
[49] Ssembatya M, Pokhrel MK, Reddy R. Simulation studies on performance of solar cooling system in UAE conditions. In: 2nd international conference on solar heating and cooling for buildings and industry (SHC), Freiburg, GERMANY; 2013. p. 1007–16.
[50] Syed A, Izquierdo M, Rodriguez P, Maidment G, Missenden J, Lecuona A, et al. A novel experimental investigation of a solar cooling system in Madrid. Int J Refrig 2005;28:859–71.
[51] Alam KCA, Saha BB, Akisawa A. Adsorption cooling driven by solar collector: a case study for Tokyo solar data. Appl Therm Eng 2013;50:1603–9.
[52] Chang WS, Wang CC, Shieh CC. Design and performance of a solar-powered heating and cooling system using silica gel/water adsorption chiller. Appl Therm Eng 2009;29:2100–5.
[53] Chen CJ, Wang RZ, Xia ZZ, Kiplagat JK, Lu ZS. Study on a compact silica gel-water adsorption chiller without vacuum valves: design and experimental study. Appl Energy 2010;87:2673–81.
[54] Hassan AA, Elwardany AE, Ookawara S, El-Sharkawy II. Performance investigation of a solar-powered adsorption-based trigeneration system for cooling, electricity, and domestic hot water production. Appl Therm Eng 2021;199:117553.

[55] Leong KC, Liu Y. Numerical study of a combined heat and mass recovery adsorption cooling cycle. Int J Heat Mass Transf 2004;47:4761–70.
[56] Lu ZS, Wang RZ, Xia ZZ, Lu XR, Yang CB, Ma YC, et al. Study of a novel solar adsorption cooling system and a solar absorption cooling system with new CPC collectors. Renew Energy 2013;50:299–306.
[57] Pan QW, Peng JJ, Wang H, Sun HQ, Wang RZ. Experimental investigation of an adsorption air-conditioner using silica gel-water working pair. Sol Energy 2019; 185:64–71.
[58] Pan QW, Wang RZ, Wang LW, Liu D. Design and experimental study of a silica gel-water adsorption chiller with modular adsorbers. Int J Refrig 2016;67:336–44.
[59] Wang DC, Wu JY, Xia ZZ, Zhai H, Wang RZ, Dou WD. Study of a novel silica gel-water adsorption chiller. Part II experimental study. Int J Refrig 2005;28:1084–91.
[60] Yu Y, Pan QW, Wang LW. A small-scale silica gel-water adsorption system for domestic air conditioning and water heating by the recovery of solar energy. Front Energy 2020;14:328–36.
[61] Gil B, Kasperski J. Performance analysis of a solar-powered ejector air-conditioning cycle with heavier hydrocarbons as refrigerants. In: ISES solar world congress (SWC), Cancun, MEXICO; 2013. p. 2619–28.
[62] Guo J, Shen HG. Modeling solar-driven ejector refrigeration system offering air conditioning for office buildings. Energ Buildings 2009;41:175–81.
[63] Pridasawas W, Lundqvisti P. A year-round dynamic simulation of a solar-driven ejector refrigeration system with iso-butane as a refrigerant. Int J Refrig 2007;30: 840–50.
[64] Tashtoush B, Alshare A, Al-Rifai S. Hourly dynamic simulation of solar ejector cooling system using TRNSYS for Jordanian climate. Energ Convers Manage 2015; 100:288–99.
[65] Vidal H, Colle S, Pereira GD. Modelling and hourly simulation of a solar ejector cooling system. Appl Therm Eng 2006;26:663–72.
[66] Bourdoukan P, Wurtz E, Joubert P. Experimental investigation of a solar desiccant cooling installation. Sol Energy 2009;83:2059–73.
[67] Joudi KA, Dhaidan NS. Application of solar assisted heating and desiccant cooling systems for a domestic building. Energ Convers Manage 2001;42:995–1022.
[68] Li H, Dai YJ, Kohler M, Wang RZ. Simulation and parameter analysis of a two-stage desiccant cooing/heating system driven by solar air collectors. Energ Convers Manage 2013;67:309–17.
[69] Mei L, Infield D, Eicker U, Loveday D, Fux V. Cooling potential of ventilated PV facade and solar air heaters combined with a desiccant cooling machine. Renew Energy 2006;31:1265–78.
[70] White SD, Kohlenbach P, Bongs C. Indoor temperature variations resulting from solar desiccant cooling in a building without thermal backup. Int J Refrig 2009;32: 695–704.